Macromolecules
ARTICLE

Macromolecules **2010**, *43*, 8191–8201 **8191**
DOI: 10.1021/ma1018632

Stability and Surface Topography Evolution in Nanoimprinted Polymer Patterns under a Thermal Gradient

Yifu Ding,*,† H. Jerry Qi,† Kyle J. Alvine,‡ Hyun Wook Ro,§ Dae Up Ahn,† Sheng Lin-Gibson,§ Jack F. Douglas,§ and Christopher L. Soles*,§

†*Department of Mechanical Engineering, University of Colorado at Boulder, Boulder, Colorado 80309-0427,* ‡*Energy and Environment Directorate, Pacific Northwest National Laboratory, Richland, Washington 99352, and* §*Polymers Division, National Institute of Standards and Technology Gaithersburg, Maryland 20899-8541*

Received August 16, 2010

ABSTRACT: Nanostructures created in polymer films by nanoimprint lithography are subject to large stresses, both those from the imprinting processes as well as stresses arising from the intrinsic thermodynamic instabilities. These stresses can induce nanostructure deformations that compromise the intended function of the imprinted pattern. Controlling these stresses, and thus the stability of the imprinted patterns, is a key scientific issue for this technology. The requirement of film stability against dewetting requires the use of entangled polymer films, which necessitates an understanding of complex viscoelastic response of these materials to large stresses. Here we investigate the evolution of the surface topography of nanoimprinted patterns in polystyrene films through a high throughput annealing approach in which the patterns are annealed for a fixed time on a controlled temperature gradient. Using principles of time−temperature superposition we systematically explore the effect of varying basic system variables such as pattern feature size, polymer molecular mass, imprinting temperature, on nanopattern stability, and on the evolution of imprinted patterns driven by surface tension and internal stress. Nanostructure collapse generally occurs through a combination of a "slumping" instability, where the imprinted film simply relaxes toward a planar film and the pattern height decreases with time, and a lateral "zigzag" instability in the nanoimprinted lines.

1. Introduction

Understanding the physical properties of polymers in thin films and nanostructures is critical for a broad spectrum of emerging nanotechnologies. One prominent example is nanoimprint lithography (NIL) which utilizes polymers to replicate features as small as a few nanometers via either a thermal embossing[1−5] or UV cross-linking[6−10] processes. In the UV form of NIL, the features on a mold are replicated by cross-linking a low viscosity liquid that has impregnated the cavities of the nanoimprint mold or template. In contrast, the thermal embossing form of NIL, or TE-NIL, relies upon viscoelastic deformations of a polymer at elevated temperatures to fill the mold cavities. While the materials used for UV-NIL are designed specifically as sacrificial resists for pattern transfer, TE-NIL has the advantage of being able to directly pattern almost any material that can be melt processed, including a range of functional materials. This eliminates the need to transfer a sacrificial resist pattern into a functional material through subsequent additive or subtractive processes.

TE-NIL processes typically require pressures on the order of several MPa and temperatures above the thermal transitions (glass transition or melting) of polymers to induce the flow of polymer into the mold cavities. This can in some cases generate strong nonlinear viscoelastic deformations of polymer which lead to significant amounts of residual internal stresses in the imprinted patterns.[11−15] These residual stresses can induce dimensional changes or distortions of the patterns over time which have deleterious effects on the performance of the imprinted nanoscale devices.[16] In addition to these processing-induced stresses, imprinted polymer nanostructures are inherently subject to surface and interfacial stresses which become increasingly dominant as the feature size decreases. These stresses raise serious concerns for the long-term stability of the patterned polymer nanostructures, particularly when the polymer is effectively "softened" by elevated temperatures, or exposure to liquid or vapor environmental contaminants, or even possibly finite size or confinement effects.

It is critical to understand how the viscoelastic nature of the imprinted polymers leads to residual stresses and how these stresses in turn impact the stability of the imprinted nanostructures. Constitutive equations of polymer rheology have been extremely important for optimizing extrusion, injection molding, and other forms of melt processing of bulk polymers. Developing similar relations, however, is a challenge for NIL processes because of the nanoscale volumes of mold cavities. At these length scales, confinement effects become prevalent and the material response can deviate from the bulk. It is difficult to perform quantitative experiments on nanoscale "samples" and establish trends over a large parameter space. In the present work, we develop a simple gradient thermal annealing approach to rapidly probe the viscoelastic response of NIL patterned polymeric nanostructures over a range of conditions. As-imprinted polystyrene (PS) patterns are annealed under a controlled temperature gradient for a fixed period of time. By analyzing the evolution of the pattern dimensions or the surface topography at different temperatures across the gradient, we rapidly identified three distinct mechanisms that impact the stability of the nanoscale pattern. The interplay of these mechanisms can be mediated through the nanoimprint temperature, pattern size, and the molecular mass of the polymer.

2. Experimental Section

2.1. NIL Process. Two PS materials, one having a molecular mass of 18,700 g/mol with polydispersity 1.02 and the other a

*Corresponding author. E-mail: Yifu.Ding@Colorado.Edu; Christopher.soles@nist.gov.

Published on Web 09/16/2010

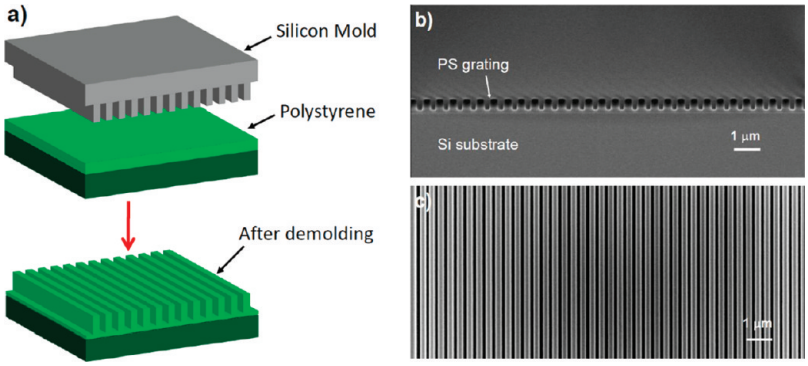

Figure 1. Fabricating polymer nanostructures via NIL process: (a) Schematic illustration of the NIL process: the features on a Si mold are replicated onto a spun cast polystyrene film. Representative SEM images of the imprinted PS19k grating with $\Lambda = 420$ nm: (b) cross-sectional view and (c) top-down view. Both SEM images are obtained without metal coating.

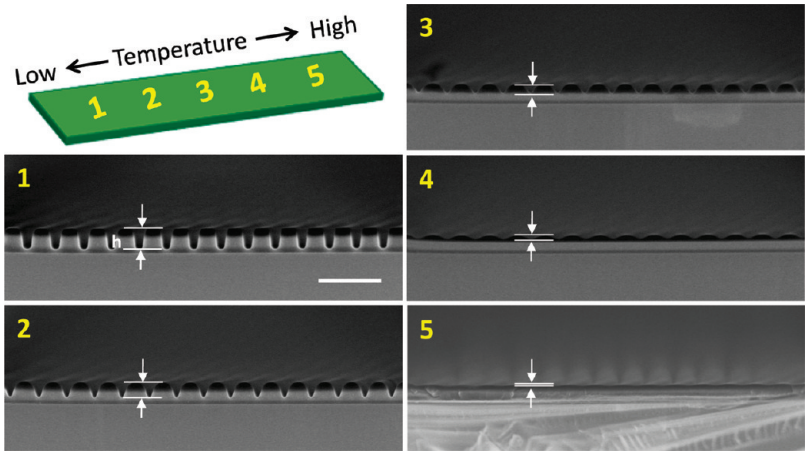

Figure 2. Formation of pattern height gradient on imprinted PS via annealing under a temperature gradient. Top left: schematic of the pattern under the temperature gradient. Cross sectional SEM of PS19k at five approximate positions (numbered 1−5) along the temperature gradient. The scale bar represents a length of 1 μm. All SEM measurements are obtained without metal coating.

molecular mass 1,510,000 g/mol and a polydispersity 1.04 were used in this study. They are referred to as PS19k and PS1.5 M throughout the remainder of the paper. Both were purchased from Scientific Polymer Products Inc., and used as received. Glass transition temperatures (T_g) were determined to be (100 ± 1) °C [The error bars presented throughout this manuscript indicate the relative standard uncertainty of the measurement.] and (106 ± 1) °C, respectively for PS19k and PS1.5 M with differential scanning calorimetry at a heating rate of 10 °C/min.

PS films with a thickness ~300 nm were prepared on Si wafers by spin coating (2000 rpm for 1 min) the PS from toluene solutions. Prior to the spin coating, wafers with a thin native oxide surface were treated in a UV-ozone cleaner (Jelight, model 42) for 1 min to remove residual organic contaminants. The as-cast PS films were then annealed in a vacuum oven at 150 °C for 1 h to remove residual toluene. NIL patterning was performed on a Nanonex NX-2000 tool. The mold consisted of silicon oxide line-space gratings with two different periodicities (or pitch), $\Lambda = 420$ and 800 nm. The line-to-space ratio of both mold patterns was approximately 2:3, meaning that the replicated PS patterns had a line-to-space ratio of 3:2. Each pattern has a field size of 20 mm × 5 mm. Mold release was facilitated with a low surface energy self-assembled monolayer, CF_3-$(CF_2)_5(CH_2)_2SiCl_3$, which was applied to the mold via a vapor deposition process.[17]

As schematically illustrated in Figure 1, the NIL patterning for each PS was performed at two separate temperatures: 20 and 80 °C above the respective T_g of each PS, both under a pressure of 3.4 MPa for 3 min. The imprinted patterns, with the mold still in contact, were cooled to 55 °C before releasing the pressure. When the mold was separated from the PS patterns, the as-imprinted PS gratings had a height $H \approx 310$ nm with a residual layer thickness $d_{RL} \approx 100$ nm. Representative field emission−scanning electron microscope (FE-SEM) images of as-imprinted PS19k grating with $\Lambda = 420$ nm are shown in Figure 1b,c. Faithful pattern replication is evident: the height of the imprinted PS patterns matches the depth of the mold cavity and the imprinted patterns exhibit sharp corners.

2.2. Thermal Annealing under a Temperature Gradient. A custom-built temperature gradient stage was used for the annealing experiments.[18] This stage consists of an aluminum platen (100 mm × 150 mm × 5 mm), a cartridge heater (controlled by a proportional-integral-derivative (PID) temperature controller, with a feedback thermocouple attached on top of the aluminum platen) embedded at one end, and a refrigerated constant temperature circulator (VWR 1165, Polyscience Inc.) at the other. After equilibrating for about 1 h, a stable linear temperature gradient was established across the central portion of the aluminum platen. The slope of gradient is determined by the total heat flux passing from the high to the low temperature side of the stage and can thus be adjusted by controlling the two set points. The imprinted PS gratings were placed on the stage with the long dimension of the patterned field (20 mm) parallel to the direction of the temperature gradient (schematically illustrated in Figure 2). Each grating was annealed for a fixed period of time before being taken off the stage, and cooled rapidly to room temperature. The details of temperature gradient, annealing temperature range, and annealing times are given in the later sections.

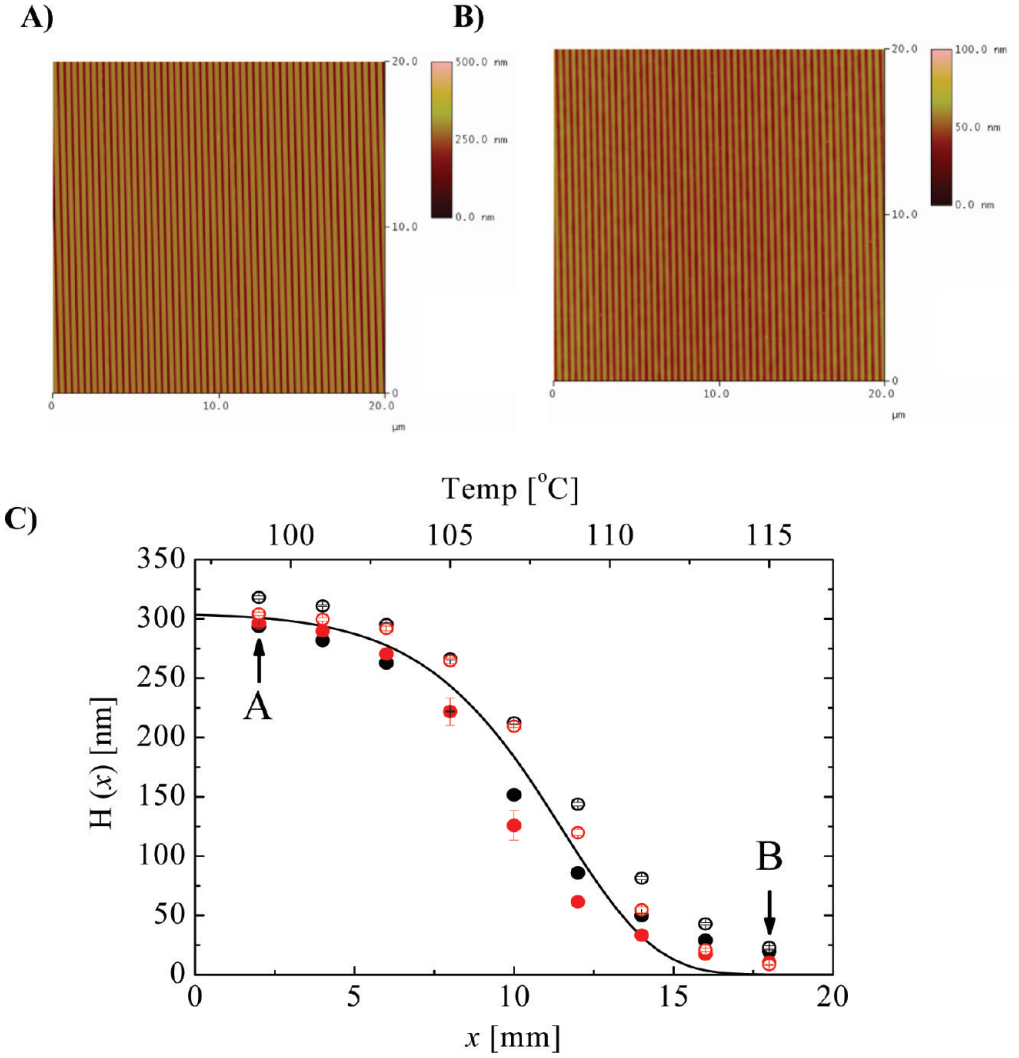

Figure 3. AFM measurements on annealed PS19k patterns. Top-down view AFM image for annealed PS19k at position, (A) x = 2 mm and (B) x = 18 mm, as marked in panel C. (C) Pattern height ($H(x)$) as a function of position (x, bottom) or annealing temperature (T, top) for PS19k gratings under a linear gradient (1.0 °C/mm) between 97 and 117 °C. The solid and empty symbols correspond to Λ = 420 and 800 nm, and black and red symbols correspond to patterns that were imprinted at 120 and 180 °C. The annealing time was 2 and 4 min for all the 420 and 800 nm patterns, respectively. Each point is an average of three measurements, and the error bars represent the standard deviations. The line represents the predictions from eq 4.

3. Results and Discussion

When the large area PS gratings are annealed on the gradient for temperatures above and around the T_g of the PS, a gradient in surface topography forms along the direction of the thermal gradient. The patterned PS at the high temperature end of the gradient have more mobility and are subsequently able to decay in the height more significantly. The resulting surface topology was then characterized by atomic force microscopy (AFM, DI3100, Veeco) as a function of position along the gradient. Two different modes of pattern decay were observed, a simple vertical decay where the lines decrease in height ("slumping"),[13] and a lateral "zigzag" undulation[19] where the lines periodically displace from the center point. In section 3.1 we focus on the vertical decay mechanism, whereas in section 3.2 we address the zigzag instability.

3.1. Vertical Pattern Height Gradient after Annealing: "Slumping". (*1*). *PS19k Patterns*. Figure 2 shows FE-SEM cross sections of a PS19k line-space grating (Λ = 420 nm, imprinting temperature, T_{imp} = 120 °C) at 5 different positions (schematically marked in the left corner of Figure 2) along the temperature gradient. The temperature gradient here is 1 °C/mm, between 97 and 117 °C. Because no conductive coatings were used for the FE-SEM measurements, some charging effects are evident in the images. Nevertheless, Figure 2 demonstrates that the height of the PS19k grating decreases gradually with an increase of annealing temperature while Λ remains constant. In addition to the FE-SEM cross sections, AFM is also used to quantify the pattern heights across the gradient at discrete increments of 2 °C. At each temperature, three measurements were taken at three different spots (with identical x), and the average values are reported here.

Figure 3 shows the pattern heights $H(x)$ for PS19k grating as a function of position x (or annealing temperature, upper axis) along the temperature gradient. Total annealing times were 2 and 4 min respectively for the patterns with Λ = 420 and 800 nm. Figure 3a,b shows representative AFM images for the annealed patterns at the low and high temperature side of the thermal gradient, respectively. Rounding of the sharp as-imprinted corners is evident while the lines remain parallel as $H(x)$ decreases toward the high temperature end (Figure 3b). This is consistent with the cross sections observed in the FE-SEM measurements (Figure 2). It is evident in Figure 3c that the gradient induced evolution of $H(x)$ does not depend upon Λ or T_{imp} for the PS19k patterns. It is important to note that the samples with 800 nm pitch were annealed twice as long as the 400 nm pitch in all of the data.

In the following, we show that this similarity is predicted by a surface tension driven viscous flow mechanism governing the pattern decay.

Our recent isothermal annealing measurements on a low molecular mass polymer, like the PS19k here, showed that the deformation process that contributes to the cavity filling during the imprint process is predominantly a Newtonian-like viscous flow.[13] This was true even for T_{imp} as low as 120 °C (only 20 °C above T_g of PS) because the terminal relaxation time (on the order of seconds) of the low molecular mass polymer is significantly shorter than the duration of imprinting (3 min). As a result, internal stresses are not frozen into the pattern as it is quenched back into the glassy state. Upon thermal annealing above T_g, when flow is enabled, the PS19k grating will smooth out toward a flat film according to a classic surface tension driven viscous flow, i.e., the surface tension, γ, induced Laplace pressure ($P \approx 2\pi^2\gamma H/\Lambda^2$) is the thermodynamic driving force toward a smooth film while the viscosity, η, of PS19k is the kinetic resistance.[20] For a simplified shape like sinusoidal profile, at a annealing temperature, $T > T_g$, H decreases exponentially with time, t[21]

$$dH/dt = (-\pi\gamma H/2\Lambda\eta) \quad (1)$$

The η of a polymer depends exponentially on T in the supercooled region in the vicinity of T_g, as typically described by the Vogel−Fulcher−Tammann equation[22,23]

$$\eta = A \exp\left(\frac{B}{\alpha_f(T - T_\infty)}\right) \quad (2)$$

where A is the structure factor, which is a strong function of the molecular mass, B/α_f is an empirical constant, and T_∞ is the Vogel temperature.[23] Here we combine eqs 1 and 2 to describe how H depends on the annealing temperature, T

$$H = H_0 \exp\left(-\frac{\pi\gamma t}{A\Lambda \exp\{B/[\alpha_f(T - T_\infty)]\}}\right) \quad (3)$$

where H_0 is the pattern height prior to annealing. Given the linear temperature gradient, $T(x) = kx + T_0$, where T_0 is the lower temperature at position $x = 0$, and k is the slope of the temperature gradient, one obtains the pattern height as a function of position across the gradient, i.e., $H(x)$

$$H(x) = H_0 \exp\left(-\frac{\pi\gamma t}{A\Lambda \exp\left(B/[\alpha_f(kx + T_0 - T_\infty)]\right)}\right) \quad (4)$$

From eq 4, $H(x)$ can be directly predicted with literature values for VFT parameters of PS19k: $B/\alpha_f = 1620$ K, $A = 5.90 \times 10^{-4}$ Pa s, and $T_\infty = 317$ K.[23] The predicted $H(x)$, and thus $H(T,t)$, for the different gratings is shown in Figure 3c and agrees well with the experimental data. Equation 4 also predicts that the $H(x)$ should be similar between the 420 nm pattern annealed for 2 min and the 800 nm pattern annealed for 4 min, because the ratio of t/Λ is almost identical. It is noted that for PS19k patterns with the same Λ, the $H(x)$ profiles do not depend on T_{imp}, consistent with the earlier studies that the mold filling process for PS19k at both temperatures agree with expectations for an Newtonian fluid.[13] In the next section, we describe more complex results from annealing of the imprinted highly entangled PS1.5 M patterns.

(*2*). *PS1.5 M Patterns*. Figure 4 illustrates the corresponding evolution of $H(x)$ for the PS1.5 M patterns after annealing

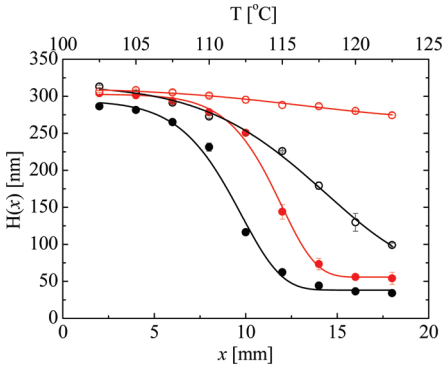

Figure 4. Pattern height ($H(x)$) as a function of position (x, bottom) or temperature (T, top) after annealing under a linear temperature gradient (1.25 °C/mm) between 100 and 125 °C for PS1.5 M gratings. The solid and empty symbols correspond patterns with $\Lambda = 420$ nm and $\Lambda = 800$ nm, and black and red symbols correspond to patterns that were imprinted at 20 and 80 °C above the T_g of the PS. The annealing time was 2 and 4 min for all of the 420 and 800 nm patterns, respectively. Each point is an average of three measurements, and the error bars represent the standard deviations. The lines represent fitting curves based on eq 5.

under a temperature gradient of 1.25 °C/mm between 100 and 125 °C. The annealing time was 2 and 4 min for the 420 and 800 nm patterns, respectively. Unlike the PS19k (Figure 3), $H(x)$ of PS1.5 M depends strongly on both Λ and T_{imp} for the annealing time stated. For a given pitch, Λ, the $H(x)$ curves (Figure 4) shift toward the lower temperature side of the gradient for the patterns with lower T_{imp}; for a given T_{imp}, the $H(x)$ decay is more dramatic for the 420 nm pattern annealed for 2 min than the 800 nm pattern annealed for 4 min. Evidently the pattern decay mechanism is more complicated than simple surface tension driven viscous flow.

For a highly entangled polymer such as PS1.5M, the rapid deformation rate (relative to the polymer chain relaxation time) imposed on the polymer during the NIL process can give rise to large levels of internal stresses.[11−15,24] The stress relaxation time or the time scale for the distorted chains to recover their equilibrium conformations depends strongly on temperature.[25] At $T_{imp} = 126$ °C, this time scale is several orders of magnitude longer than our NIL processing time (3 min). These unrelaxed stresses will be frozen into the imprinted pattern once the sample is quenched below T_g; when the patterns are heated back to (or above) T_g without the confinement and pressurization from the mold, these internal stresses are released and drive an elastic recovery of the polymer in the opposite direction of the flow to fill the mold, i.e., a rapid decay in pattern height. The magnitude of these internal stresses, determined by how rapidly the polymer chains can recover their equilibrium conformations during the NIL process, decreases as T_{imp} increases.[25] Thus, the internal stress of the PS1.5 M patterns with a given Λ are anticipated to be higher for patterns imprinted at 126 °C than at 186 °C, causing a shift of the $H(x)$ curves toward the low temperature side (Figure 4) of the gradient for the patterns having a lower T_{imp}.

The exact time scale for the internal stress relaxation of the PS1.5 M patterns is difficult to estimate given our incomplete understanding of the polymer entanglement. However, some phenomenology is established that can guide us in making practical estimates. For example, it has been shown that the time required for disentangled polymer chains, subjected to strong flows that greatly reduce their shear viscosity, to recover to their equilibrium or steady state takes about 1.5 orders of magnitude longer than the terminal relaxation time, τ_1.[26] A complication in the present situation is that the polymer

relaxation times may deviate from their bulk values either through the effects of confinement at equilibrium or chain disentanglement under flow.[27,28] Nonetheless, we can expect the internal stresses for a given T_{imp} to be larger in the 420 nm imprint patterns than in the 800 nm patterns. This is because deformation rate, $\dot{\gamma}$, associated with material flowing into the mold during the imprint process scales as $\dot{\gamma} = 3sv/h^2$, where h is the film thickness, s is the width of the extruded part of the mold, and v is the advancing velocity of the mold.[29,30] For films with similar h, s is smaller (~160 nm) for the 420 nm pattern than that (~400 nm) in the 800 nm patterns, meaning that the imposed $\dot{\gamma}$ is larger for the 420 nm pattern. We also anticipate that the time for the chains to restore their equilibrium conformation could be longer in smaller cavities whose surface-volume ratio is large due to higher degree of interfacial interactions. This "slowed" chain relaxation time could also enhance the residual stress effects induced by imprinting and correspond to a faster decay in the smaller imprinted patterns upon annealing. Lastly, in addition to the residual stress, the 420 nm patterns have a surface tension induced Laplace pressure that is ~3.6 times greater than the 800 nm patterns with the same pattern height, simply due to the smaller radius of curvature in the finer scale pattern. Even though the viscous flow of the high molecular mass PS is significantly slower than PS19k, these mechanisms will also contribute to higher pattern decay rate.

To quantitatively analyze our observations on the imprinted entangled polymer films, we fit the $H(x)$ profiles in Figure 4 with the assumption that both the internal stresses arising from imprinting and Laplace pressure induced stresses result in a reduced viscosity (η_{eff}) of the PS film. This is a problem that essentially does not arise in the unentangled polymer film. Additionally, the patterned PS1.5 M is likely to have a heterogeneous distribution of mobility associated with local fluctuations in the chain entanglement.[31] Douglas and Hubbard (DH) introduced a model of chain entanglement that predicts that high molecular mass polymer melts are dynamically heterogeneous, in much the same fashion as glass forming liquids, albeit at a much larger length scale where the primary fluid elements are the polymer chains.[32,33] According to the DH model, a stretched exponential stress relaxation resulting from the dynamic heterogeneity of polymer melts rather than a simple exponential relaxation shown in eq 1 and we adopt this form in our analysis of the entanglement relaxation. In particular, the gradient patterns in Figure 4 are fit to the relation,

$$H(x) = (H_0 - H_\infty)\exp\left(-\left(\frac{\pi\gamma t}{A\Lambda\exp\left(B/[\alpha_f(kx + T_0 - T_\infty)]\right)}\right)^{\beta}\right) \quad (5)$$

where H_0 is the as-imprinted pattern height, H_∞ is the pattern height at the high temperature side of the gradient, and β is the stretching parameter. In this equation we can roughly estimate H_0 and H_∞ from the experimental data in Figure 4. It is generally accepted that B/α_f (=1620 K) and T_∞ (=48.4 °C) are invariant with the processing conditions and molecular mass for highly entangled PS.[23] That leaves A and β as the only two remaining fitting parameters. The best fit to the $H(x)$ curves, determined by statistical significance, for all the experimental data of PS1.5 M are plotted in Figure 4. The results of the fit parameters are reported in Table 1.

From Figure 4, a "plateau" like pattern height is encountered at the high temperature side of the gradient, coincident with our definition of H_∞. The apparent H_∞ increases with both Λ and T_{imp} for the annealing time given. For the PS1.5 M pattern with Λ = 800 nm and T_{imp} = 186 °C, $H_\infty \approx$ 268 nm which means that after annealing for 4 min at 122.5 °C, the pattern height reduces only by ~14%. The level of H_∞ reflects the degree of internal stresses within the patterned lines: the percentage of patterns that remained after initial quick elastic recovery. The values of A obtained for all the patterns are in the range of 10^{-4}–~10^{-3} Pa s (Table 1), suggesting that the PS1.5 M actually shows comparable effective mobility to PS19k ($A \approx 10^{-4}$ Pa s) in response to the thermal annealing. Such a value is 5–6 orders of magnitude smaller than the Newtonian structural factor, A_N, of PS1.5 M (~170 Pa s), and is close to the A_N of a PS with a molecular mass around 20k–50k.[23] This dramatic enhancement in mobility is impossible to justify only using the Laplace pressure induced thinning effect. The initial (and largest) Laplace pressure associated with the grating pattern is on the order of 1 MPa, which is certainly larger than the critical stress for the onset of shear thinning for PS1.5 M melts within the range of annealing temperatures experienced here.[34] However, such a pressure is not high enough to induce approximately a 6 orders magnitude reduction in viscosity. Shear deformation is known to reduce η with $\dot{\gamma}$ according to the Carreau equation, $\eta = \eta_\infty + (\eta_0 - \eta_\infty)[1 + (\tau_T\gamma)^2]^{(n-1)/2}$ where τ_T is a time constant and n is the power law exponent.[35,36] A reduction of viscosity by ~6 orders of magnitude would necessitate that the Laplace pressure created an equivalent shear rate of ~10^{17} s^{-1} (assuming $\eta_\infty = 0$, τ_T = 11 s, and n = 0.67), which is a unrealistically high value. Furthermore, Porter et al. have shown that high stresses or deformation rates can cause the chains to fully disentangle and the scaling relationship between η (similarly for A) and molecular mass (M) changes from $M^{3.4}$ to M^{1}.[37] Even under such an extreme scenario, the lowest possible η and A for a fully disentangled PS1.5 M would still be ~70 times greater than the PS19k.

Table 1. Parameters Obtained by Using eq [5] to Fit the Pattern Height Gradient in PS1.5M

	T_{imp} = 126 °C		T_{imp} = 186 °C	
	Λ = 420 nm	Λ = 800 nm	Λ = 420 nm	Λ = 800 nm
H_0 [nm]	293.9	314.3	302.6	311.0
H_∞ [nm]	38.2	59.6	55.6	267.9
β	0.99	0.57	1.24	0.42
A [Pa s]	3.1×10^{-4}	3.3×10^{-3}	8.7×10^{-4}	2.6×10^{-3}

As discussed above, a plausible explanation of our observations for the PS1.5 M sample is that the highly deformed entangled pseudonetwork during the NIL processes induces entropic elasticity effects. Polymers in their rubbery entangled network state are known to display hyper-elastic deformations up to several hundred percent strains. It is conceivable that these materials accommodate large elastic deformations during the cavity filling process and that the resulting stresses would be retained in the patterns if sufficient time is not allowed for these elastic distortions to relax. Viscous flow, possibly nonlinear in nature, will also contribute to the generation of internal stresses during pattern formation. It is hard to envision the formation of such sharp corners of the imprinted patterns if only elastic deformation is involved. The subsequent pattern evolution upon annealing at elevated temperatures is inevitably convoluted with the elastic stress and surface tension driven flow phenomena. From a qualitative standpoint, we expect the relative contributions of the entropic elastic deformation will decrease with an increase of T_{imp}, accompanied by a concomitant increase

of the viscous contribution. Therefore, the rapidly responding pattern profiles (small A) in Figure 4 is likely due to the elastic recovery of highly deformed polymer network. In this regime the response is controlled by a characteristic molecular mass related to the development of a transient chain entanglement network; this critical mass is designated either M_e (molecular mass between entanglement junctions) or by the related quantity M_c (critical molecular mass marking the transition from unentangled to entangled regimes, $M_c \approx 2 M_e$).[25] For PS, $M_e \approx 15$ k and $M_c \approx 30$ k,[38] both of which are comparable to observed values of $A \approx 20\text{k}-50\text{k}$.

With an increase of T_{imp}, the viscous contribution of PS1.5 M to the total cavity filling processes must increase, allowing for more relaxation of the deformed network. For the conditions employed here, the patterns with $\Lambda = 800$ nm and $T_{imp} = 186$ °C should have the largest ratio of viscous to elastic deformation involved in the imprint process. This is consistent with the observation that after annealing these patterns on the 100−125 °C gradient for 4 min, very little pattern decay is observed; the pattern height $H(x)$ varies from approximately 311 to 268 nm across the gradient, as seen Figure 4 and detailed in Table 1. Without significant internal stresses or elastic recovery, the pattern decay will be driven by the surface tension which is exceedingly slow given the large viscosity of the PS1.5 M at these annealing temperatures.

From Table 1, the stretching exponents β for all different patterns are smaller than 1, except for the PS1.5 M with $\Lambda = 420$ nm and $T_{imp} = 186$ °C. A value of $\beta < 1$ is consistent with the expected heterogeneous distribution of mobility within the polymer melt, as discussed above, whereas a value of $\beta > 1$ is characteristic of the "abnormal" stress relaxation in systems that contain complicated or dynamically heterogeneous structure such as aging gels or polymer nanocomposites.[39−41] As we will elaborate in the next section, this abnormal β results from an additional pattern decay mechanism. This mechanism was first observed in our recent isothermal annealing study for the PS1.5 M with $\Lambda = 420$ nm and $T_{imp} = 186$ °C where a "zigzag" type or lateral instability occurs along each imprinted PS lines during the thermal annealing.[19] We have discussed this zigzag instability previously in terms of a capillary instability that lowers the effective surface area.[19,42] However, the origin of this zigzag instability remains unclear. In the next sections, we describe a detailed experimental and theoretical analysis that incorporates the compressive stresses that potentially induce such zigzag instability.

3.2. Zigzag Instabilities. (*1*). *Experimental Analysis*. As mentioned above, for PS1.5 M patterns with $\Lambda = 420$ nm and $T_{imp} = 186$ °C (referred to as PS1.5M_SH for convenience), the stretching parameter β obtained from fitting the height decay data is larger than 1 (Table 1), indicative of complicated relaxation processes. This is evident in the AFM image of the PS1.5M_SH (Figure 5) after a relatively brief annealing, where we observe a "zigzag" undulation that occurs simultaneously with the pattern height decay. The undulations in neighboring lines are roughly 90° out of phase and appear to coalesce upon further annealing. The temperature gradient annealing methods introduced here provides an ideal experimental means to track the onset and evolution of this lateral undulation. Figure 6a shows topographic AFM images of the annealed PS1.5M_SH at different positions along the gradient, or annealing temperatures, as indicated on each image. In this case the temperature gradient was 1.25 °C/mm, between 100 and 125 °C. For temperatures lower than 113 °C, lateral undulations are not yet observed and the PS lines only show a gradual reduction

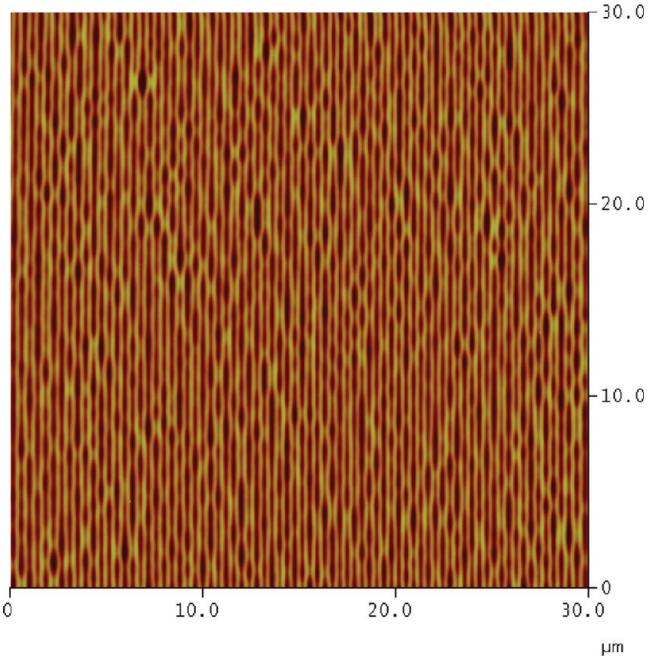

Figure 5. Typical topographic AFM image of the "zigzag" lateral instabilities observed in the annealed PS1.5M_SH at the high temperature side of the annealing stage.

in height. Above 115 °C, however, the PS lines start to undulate and develop the "zigzag" pattern with the amplitude of the waviness increasing with annealing temperature. Now we quantify the geometrical characteristics of this pattern formation. We point out for completeness that annealing at the lower temperatures (still above T_g) for similar patterns did eventually lead to the instability after longer term annealing.[19]

The evolution of these undulations can be quantified by calculating the 1D power spectrum density (PSD) of the AFM images along the direction parallel to lines, as shown in Figure 6b. At the low temperature side of the gradient (100−113 °C) lateral undulations are not observed and the PSDs display a power law dependence on the wave vector with a scaling exponent between −1.8 and −2.0. For these laterally uniform gratings, height variations are not observed and there is no contrast in the AFM image in the direction along the grating lines. The PSDs for these featureless structures are typical of a white noise power law spectrum with an exponent of −2.0. As the annealing temperature exceeds 115 °C, a "scattering peak" (at $q < q_c \approx 6-7\ \mu\text{m}^{-1}$) appears above the white noise spectrum, and the amplitude of this correlation peak increases with the annealing temperature (Figure 6b). To extract the correlation length (or undulation wavelength) associated with the peak, we subtracted the background of the PSD spectra for annealing temperatures from 115 °C −123 °C.[43] This background consisted of both the white noise (power law) and a low q scattering (Gaussian tail) that corresponds to large scale inhomogeneity. The resulting PSD spectra featuring the characteristic scattering peaks are shown in Figure 6c.

The characteristic wavelength λ_m associated with the scattering peak is defined as $\lambda_m = 2\pi/q_m$, where q_m is the wave vector corresponding to the peak maximum. Figure 7 displays the evolution of λ_m as a function of the annealing temperatures. Also included are the λ_m values deduced from the PS1.5M_SH annealed on a different temperature gradient (1.25 °C/mm between 105 and 130 °C for 1 min; AFM images not shown), using the same procedure described

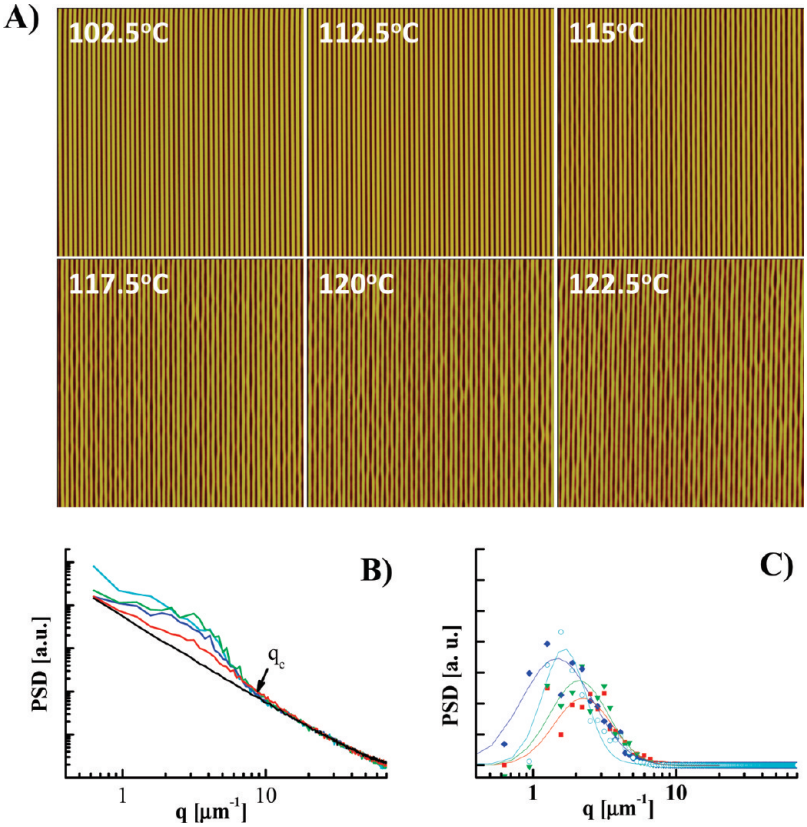

Figure 6. (A) AFM images of the annealed PS1.5M_SH at different positions (or temperatures, as marked) along the temperature gradient (1.25 °C/mm between 100 and 125 °C) for 2 min. All the AFM images are 20 μm × 20 μm. (B) 1D - PSD spectra (along the grating lines) for all the AFM images except the T = 102.5 °C shown in panel A. (C) Remaining PSD spectra after subtraction of the background, and the lines represent the log-normal fit to extract the position of the peak maximum. Different colors in B and C represent different annealing temperature: black, 112.5 °C; red, 115 °C; blue, 117.5 °C; green, 120 °C; cyan, 122.5 °C.

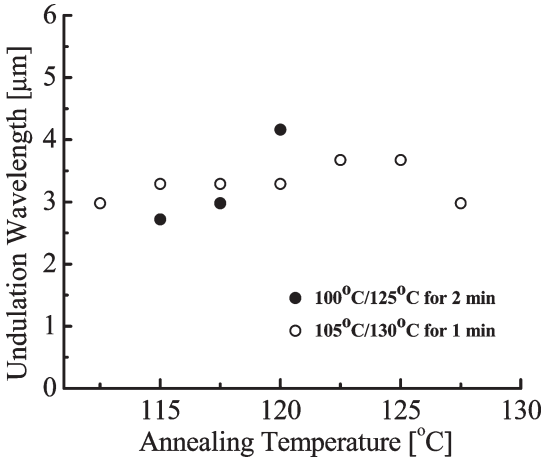

Figure 7. Wavelengths of the line undulation as a function of the annealing temperature obtained.

above. Statistically significant changes of λ_m on annealing temperature are not observed. Any variations in λ_m probably stem from the other sources of uncertainty, including the AFM measurements themselves and the background subtractions. The average value of λ_m from all of the measurements in Figure 7 is 3.3 ± 0.4 μm. We can also define a cutoff wavelength λ_c, below which the PSDs deviate from the white noise spectrum. As indicated in Figure 6b, q_c is experimentally defined as approximately 6 − 7 μm^{-1} which corresponds to a λ_c ($=2\pi/q_c$) of approximately 0.9−1.0 μm, in good agreement with our previous capillary instability model for the zigzag undulations.[19]

PS1.5 M is a highly entangled polymer that exhibits significant viscoelasticity. When this polymer is imprinted at sufficiently high temperatures (such as 186 °C), the flow induced deformations can relax significantly and the internal or residual stresses in the as-imprinted patterns are minimized. Upon annealing, a reduction of surface tension is the predominant driving force for the pattern leveling or vertical pattern height decay. However, the viscosity of the PS1.5 M polymer is extremely high near T_g and this decay mechanism can be extremely slow. It is under these conditions, where the pattern is relatively stress free, the simple vertical decay mechanism is extremely slow, and the pattern is still relatively "soft", that we observe this characteristic zigzag instability.

Previously we observed a similar lateral instability in high molecular weight PS as well as significantly lower molecular mass imprinted PS patterns of similar dimensions that were coated with a fluorinated surfactant.[19,42] The surfactant was supposed to segregate to the surface and reduce the surface tension driving force for pattern leveling and the expected viscosity reduction arising from the fluorinated additive naturally led us to model the zigzag instability in terms of a Rayleigh-Tomitika type thread break-up instability.[19] However, even in the presence of the surfactant, the viscosity of the PS1.5 M remains high, while the zigzag instability is conspicuously observed only after of annealing near T_g for a few minutes. Frankly, this behavior is hard to understand on the basis of a fluid capillary instability model, and we now believe this instability mechanism is not operative in these entangled polymer films. Instead, the model and evidence

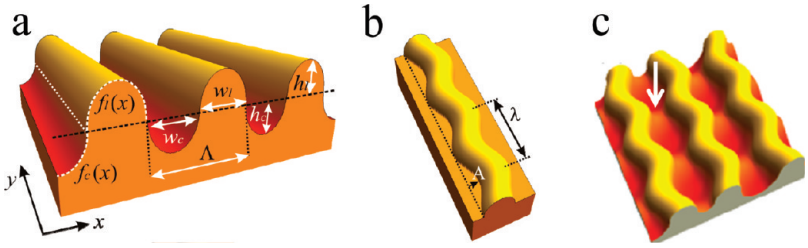

Figure 8. (a) Piece-wise construction to model the surface. Both lines $f_l(x)$ (concave down) and channels $f_c(x)$ (concave up) are described by half-elliptical cross sections. (b) The zigzag mode is defined by a sinusoidal displacement along the y direction of the center of the line (or channel). (c) The 3D surface topography of the lateral instability as a result of line undulations in panel b.

discussed in the next section supports a picture in which the undulatory patterns in the nanoimprinted entangled films arise from an elastic instability rather than a fluid instability. In the following, we develop a mechanical analysis that considers both the surface and elastic energies associated with the "zigzag" undulations under a compressive stress along the length of the lines that seems to be consistent with the characteristics of the observed lateral instability in this highly viscoelastic polymer.

(*2*). *Model of Stress-Induced Zigzag Instability*. We model the zigzag instability by combining both surface energy variations based on our previous model[19] and the elastic energy resulting from compressive stress acting along the axial direction of the lines. The origins of such a compressive remain unclear; potential candidates for such an axial compressive stress are discussed later. Nevertheless, in the high viscosity limit where the aforementioned capillary instability is kinetically not feasible, it seems that an axial compression is the only other plausible explanation for such a deformation mode of the lines. Our approach here is similar to recent studies by Huang et al. on the mechanical buckling instability of confined polymer thin films under a compressive load.[44−49]

First, we model surface area change as a consequence of the perturbation of the instability, following our recent capillary zigzag instability.[19] Figure 8a shows the geometric constructions: the surface is modeled in a piecewise-continuous fashion by separating the patterns into adjacent lines (concave down regions) and channels (concave up regions). Cross sections of both lines and channels are defined by half-ellipses with respective height h, and width w, which give a good approximation to the experimental data after the initial stages of annealing have rounded the sharp corners of the pattern. Zigzag undulations are then imposed by a perturbation of the line center defined by amplitude A and wavelength λ (Figure 8b)

$$a(y) = A \sin(2\pi y/\lambda) \tag{6}$$

To calculate the surface area associated with line undulations, we assume that the pitch Λ, line width (w_l), channel widths (w_c), and the volume of polymers within the lines (and spaces within the channels) are conserved. Volume conservation is assumed to be local: changes in line volume V_l (or channel volume, V_c) due to the perturbations are compensated for by corresponding changes in line height $h_l(A)$ (or channel height $h_c(A)$), yielding the total area of a line with original length of L_0

$$S_T \approx \frac{\pi L_0}{2}\left[\left(1+\frac{A^2\pi^2}{\lambda^2}\right)\left(h_c-\frac{A^2}{w_c}+\frac{\Lambda}{2}\right)+h_l\right] \tag{7}$$

Thus, the total surface energy change ΔU_{sur} during line undulation is

$$\Delta U_{sur} = \gamma(S_T - S_L) = \gamma\frac{\pi L_0}{2}\left(\frac{A^2\pi^2}{\lambda^2}\right)\left[\left(h_c-\frac{A^2}{w_c}+\frac{\Lambda}{2}\right)\right] \tag{8}$$

where S_L is the surface area of the grating line before the undulation occurs. For a viscoelastic polymer like PS1.5M, during line undulation, the bending energy can be expressed as

$$U_{bend} = \frac{1}{2}nEI\int_0^\lambda (a'')\,dy = \frac{E\pi^4 L_0}{3\lambda^4}{w_l}^3A^2\left[h_l\left(1+\frac{A^2\pi^2}{\lambda^2}\right)^{-1}+h_c-\frac{A^2}{w_c}\right] \tag{9}$$

where E, the effective rubbery modulus of the PS1.5M, is taken to be 0.2 MPa and I, the moment of inertia, is estimated to be ${w_l}^3(h_c + h_l)/12$. In addition to the line bending, the residual layer also deforms and stores elastic energy. Here, we assume that the residual layer deforms in a manner affine to the surface undulation

$$u_x(y,z) = A\sin(2\pi y/h)\frac{z}{d_{RL}} \tag{10}$$

The resulting elastic energy stored in the residual layer is then

$$U_{shear} = \frac{1}{24}nE\Lambda\int_0^\lambda\int_0^{d_{RL}}\left[\left(\frac{\partial u_x}{\partial y}\right)^2+\left(\frac{\partial u_x}{\partial z}\right)^2\right]dz\,dy = \frac{1}{24}E\Lambda A^2L_0\left[\frac{1}{2h_s}+\frac{2d_{RL}\pi^2}{3\lambda^2}\right] \tag{11}$$

The nature of the deformation reflected in the lateral undulations is consistent with a compressive stress along the axial direction of the lines. While the origins of this axial compressive stress have not been fully verified, as discussed later there are several possible origins for such compressive stress. For now if we assume that a compressive stress ($\bar{\sigma}$) acts along the long axis of the lines and induces undulations, the resulting work done by $\bar{\sigma}$ is

$$W_p = \frac{1}{2}Pn\int_0^\lambda (w')^2\,dy = \bar{\sigma}\frac{A^2\pi^2}{\lambda^2}w_l\left[h_l\left(1+\frac{A^2\pi^2}{\lambda^2}\right)^{-1}+h_c-\frac{A^2}{w_c}\right]L_0 \tag{12}$$

As discussed later, there are many possible sources for compressive stress. Two immediate possibilities including eigenstrain due to thermal mismatch between the PS1.5 M and the Si substrate and the flow induced stresses. At present, we do not distinguish the stresses from two possible sources and assume that they contribute in the same way to line instability. Under such circumstances, regardless of the compressive stress origin, the energy balance is

$$W_p = \Delta U_{sur} + U_{bend} + U_{shear} \tag{13}$$

which yields

$$\bar{\sigma} w_l \left[h_l \left(1 + \frac{A^2\pi^2}{\lambda^2} \right)^{-1} + h_c - \frac{A^2}{w_c} \right] - \gamma \frac{\pi}{2} \left[\left(h_c - \frac{A^2}{w_c} + \frac{\Lambda}{2} \right) \right] - \frac{E\pi^2}{3\lambda^2} w_l{}^3 \left[h_l \left(1 + \frac{A^2\pi^2}{\lambda^2} \right) + h_c - \frac{A^2}{w_c} \right] - \frac{1}{24} \lambda^2 E\Lambda \left[\frac{1}{2d_{RL}} + \frac{2d_{RL}\pi^2}{3\lambda^2} \right] = 0 \tag{14}$$

At the onset of the line undulation, the amplitude of undulation, $A \to 0$. Therefore

$$\frac{1}{48\pi^2 d_{RL}} \lambda^4 E\Lambda - \left\{ \bar{\sigma} w_l [h_l + h_c] - \gamma \frac{\pi}{2} \left[\left(h_c + \frac{\Lambda}{2} \right) \right] - \frac{1}{36} E\Lambda d_{RL} \right\} \lambda^2 + \frac{E\pi^2}{3} w_l{}^3 [h_l + h_c] = 0 \tag{15}$$

In order to obtain a real solution, the above equation requires

$$\left\{ \bar{\sigma} w_l [h_l + h_c] - \gamma \frac{\pi}{2} \left[\left(h_c + \frac{\Lambda}{2} \right) \right] - \frac{1}{36} E\Lambda d_{RL} \right\}^2 \geq \frac{E^2 \Lambda w_l{}^3}{36 h_s} [h_l + h_c] \tag{16}$$

and the critical load is obtained when the above inequality becomes equal

$$\bar{\sigma}_{crit} = \frac{\frac{E w_l}{6} \sqrt{\frac{\Lambda w_l}{h_s} [h_l + h_c]} + \gamma \frac{\pi}{2} \left[\left(h_c + \frac{\Lambda}{2} \right) \right] + \frac{1}{36} E\Lambda d_{RL}}{w_l [h_l + h_c]} \tag{17}$$

and accordingly the critical wavelength λ_{crit}, corresponding to smallest $\bar{\sigma}$ that can induce undulation is

$$\lambda_{crit}{}^2 = 4\pi^2 w_l \sqrt{\frac{d_{RL} w_l}{\Lambda} [h_l + h_c]} \tag{18}$$

assuming the geometric parameters for the imprinted PS1.5M_SH film near the onset of the instability are equal: specifically, $\Lambda = 420$ nm, $h_c = h_l = 100$ nm, $w_c = w_l = 240$ nm, $d_{RL} = 100$ nm, we predict $\lambda_{crit} \approx 1.0$ μm and a critical stress $\bar{\sigma}_c \approx 0.4$ MPa. The resulting λ_{crit} estimate under these conditions agrees rather well with the experimentally determined cutoff wavelength, $\lambda_c \approx 0.9$ to 1 μm, observed in Figure 6b. Note that experimental value also agrees well with our model only considering surface energy.[19] The characteristic wavelength of this instability as a function of $\bar{\sigma}$ is obtained by solving eq 15 with the geometric parameters indicated above, and the results are shown in Figure 9. The existence of a critical stress and a critical wavelength are evident, consistent with the elastic instability model. At $\bar{\sigma} < \bar{\sigma}_c$, instability will not occur due to the constraints from both the surface energy (ΔU_{sur}) along the lines and elastic deformation energy ($\Delta U_{bend} + \Delta U_{shear}$). When the $\bar{\sigma} > \bar{\sigma}_c$, an instability becomes possible. The two branches in Figure 9 correspond to the two possible solutions for eq 15, suggesting that for the same $\bar{\sigma}$ there may exist two characteristic wavelengths. The longer wavelength is preferred because when the grating pattern evolves from a line (or $\lambda \to \infty$) into a wavy shape, it develops at the longer wavelength first. According to eq 15 and Figure 9, a characteristic wavelength of 3.3 μm corresponds to a compressive stress ~0.7 MPa, which is a reasonable value for a high molecular mass polymeric material near it is glass transition temperature.

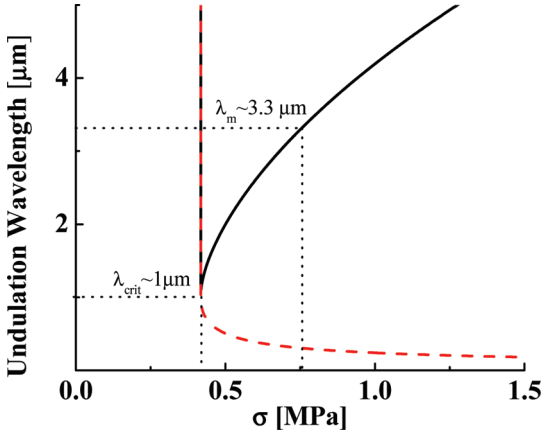

Figure 9. Wavelength as a function of the compressive stresses: red and blue lines represent two possible solutions of eq 12. The critical wavelength, λ_{crit}, is marked using the geometrical information specified in the text. The position of the characteristic wavelength, λ_m, from experimental (Figure 7) is also marked, showing the corresponding compressive stresses.

We note here that the observed lateral instability in the annealed PS1.5M_SH pattern is not purely elastic in nature. During the pattern evolution, the cross sectional profiles evolve through viscoelastic flow, and mass transport as a result of viscous deformation is clearly present. Therefore, the precise value of the compressive stress estimates may vary. Nevertheless, based on above preliminary experimental and theoretical analysis, a compressive stress could cause the patterned polymer line to undulate and result in a cutoff or critical wavelength λ_c and a characteristic wavelength λ_m depending on the magnitude of the compressive stress. The question remains: what is the origin of the compressive stress in the patterns during the annealing, and why it is unique for the PS1.5M_SH?

An obvious candidate is thermal induced stress (TIS) due to the mismatch of thermal expansion coefficient between the PS1.5 M and the Si substrate. Since the thermal expansion coefficient of the Si substrate (α_{Si}) is significantly smaller than that of the PS (α_{PS}), a compressive stress could develop in the imprinted PS lines during the heating

$$\Delta\sigma = \int_{T_1}^{T_2} \frac{E_{PS}}{1 - \nu_{PS}} (\alpha_{PS} - \alpha_{Si}) \, dT$$

where T_1 and T_2 correspond to room temperature and the annealing temperature, E_{PS} (few GPa) and ν_{PS} (~0.4) is the

modulus and Poisson ratio of the glassy PS. Considering linear thermal expansion coefficient of PS and S_i, $\alpha_{PS} = 7.2 \times 10^{-5}$ °C^{-1}, and $\alpha_{Si} = 2.5 \times 10^{-6}$ °C^{-1}, the elastic thermal stresses in the PS samples as they are heated from room temperature (25 °C) to 115 °C is around 1.3 MPa. For one-dimensional PS linear gratings, this effectively creates a lateral compressive stresses along the grating axis. Such a TIS would be equalivant for all of the PS patterns. The fact that only PS1.5M_SH shows the lateral instability, which rises after the pattern height has reduced from ~300 to ~200 nm, suggests that TIS is less likely to be the origin of the lateral instability.

The other, potentially less obvious candidate, is flow induced stresses (FIS) in this highly entangled PS1.5M. In the absence of elastic recovery, the PS1.5M_SH pattern is subjected to a surface tension induced Laplace pressure (initial value ~1 MPa), which is higher than the critical stresses for the onset of stress induced thinning effect. Under the current geometry, the enhanced flow along the vertical direction will induces large normal stresses (and recoverable strain) both parallel and perpendicular to the lines. This is the nanoscale analogue of the well-known die swell or rod climbing phenomena caused by flow induced elasticity in highly entangled polymers. This would result in the imprinted features "expanding" in the directions orthogonal to the polymer flow. However, such elastic recovery along the line direction would be highly constrained by the supporting Si substrate. This constraint would be tantamount to effectively inducing a compressive stresses along the long axis of the lines.

Following this argument, the PS1.5 M patterns with $\Lambda = 800$ nm and $T_{imp} = 186$ °C show very slight pattern height gradient, and thus a less significant nonlinear viscoelastic flow (Figure 4). This is because the Laplace pressure ($P \approx 1/\Lambda^2$) is about 4 times smaller in the 800 nm patterns than in the 420 nm patterns. Further, for PS1.5 M patterns created at 126 °C, the major driving force is the internal stresses or elastic recovery, which will not generate considerable compressive stresses along the lines. Within the narrow annealing temperature range (~25 °C) in the present study, the difference in the FIS is rather small, therefore, no significant dependence of the wavelength on the annealing temperature is expected (Figure 7).

Regardless of the origin, the instability, once initiated, keeps growing. Kinetically, once the waviness is formed, the amplitude will form a sharp curvature at the trench between two neighboring lines, which will have higher Laplace pressure than the average trench (as marked by the arrow in Figure 8c). This will draw materials to reduce the sharp curvature. Therefore it is a self-catalytic growth of the instability (Figure 7b), and also causing neighboring lines to be 90° out of phase, which eventually leads the coalescence of the lines.

4. Conclusions

In this study, we utilize an efficient combinatorial method based on a linear thermal gradient in the polymer films to probe the evolution of nanoimprinted polymer patterns under thermal annealing conditions. We find that the evolution of the surface topography of the imprinted patterns in the temperature gradient is controlled by three distinct mechanisms, each of which can become predominant under appropriate physical circumstances. For PS19k patterns, the pattern decay upon annealing is controlled by the surface tension driven viscous flow mechanism, and the degree of gradient can be predicted based on the temperature dependence of the polymer viscosity. For highly entangled PS1.5M, the pattern development is strongly dependent on the imprinting temperature T_{imp} and the pattern feature size. However, for patterns created at low temperature, near the glass transition temperature ($T_{imp} = T_g + 20$ °C), the pattern evolution is dominantly elastic recovery, a result of unrelaxed internal stresses developed during the NIL process. At high imprinting temperature ($T_{imp} = T_g + 80$ °C) when the internal stresses are largely relaxed, the patterns created will decay more slowly for larger patterns ($\Lambda = 800$ nm) or fast ($\Lambda = 420$ nm), depending on whether the surface tension induced Laplace pressure is large enough to create strong nonlinear flow. If the later is the case, a flow induced stress, compressive in nature, develops and causes the lines to become unstable through an elastic undulatory instbility. Our model of this phenomenon provides an encouraging estimation and good physical understanding of both the observed cutoff wavelength and the most characteristic wavelength.

Understanding the origin of these stability and instability is important for postfabrication processes. Unique gradient surface topographies, i.e., identical pattern pitch but continuous variation in height, are highly efficient experimental platforms for probing surface topography related phenomenon such as cellular responses,[50] liquid wetting,[51] and liquid crystal orientation.[52]

Acknowledgment. We acknowledge the funding support from the National Science Foundation under Grant Nos. CMMI-0928067 and CMMI-1031785 and the nanofabrication laboratory of the Center for Nanoscale Science and Technology (CNST) at NIST for access to their facilities.

References and Notes

(1) Austin, M. D.; Ge, H. X.; Wu, W.; Li, M. T.; Yu, Z. N.; Wasserman, D.; Lyon, S. A.; Chou, S. Y. *Appl. Phys. Lett*. **2004**, *84*, 5299.
(2) Chou, S. Y.; Krauss, P. R.; Renstrom, P. J. *Science* **1996**, *272*, 85.
(3) Chou, S. Y.; Krauss, P. R.; Renstrom, P. J. *J. Vac. Sci. Technol. B* **1996**, *14*, 4129.
(4) Guo, J. L. *Adv. Mater*. **2007**, *19*, 1.
(5) Guo, L. J. *J. Phys. D: Appl. Phys*. **2004**, *37*, R123.
(6) Bailey, T.; Choi, B. J.; Colburn, M.; Meissl, M.; Shaya, S.; Ekerdt, J. G.; Sreenivasan, S. V.; Willson, C. G. *J. Vac. Sci. Technol. B* **2000**, *18*, 3572.
(7) Resnick, D. J.; Mancini, D.; Dauksher, W. J.; Nordquist, K.; Bailey, T. C.; Johnson, S.; Sreenivasan, S. V.; Ekerdt, J. G.; Willson, C. G. *Microelectron. Eng*. **2003**, *69*, 412.
(8) Gates, B. D.; Xu, Q. B.; Stewart, M.; Ryan, D.; Willson, C. G.; Whitesides, G. M. *Chem. Rev*. **2005**, *105*, 1171.
(9) Long, B. K.; Keitz, B. K.; Willson, C. G. *J. Mater. Chem*. **2007**, *17*, 3575.
(10) Jung, G. Y.; Johnston-Halperin, E.; Wu, W.; Yu, Z. N.; Wang, S. Y.; Tong, W. M.; Li, Z. Y.; Green, J. E.; Sheriff, B. A.; Boukai, A.; Bunimovich, Y.; Heath, J. R.; Williams, R. S. *Nano Lett*. **2006**, *6*, 351.
(11) Scheer, H. C.; Bogdanski, N.; Wissen, M.; Konishi, T.; Hirai, Y. *J. Vac. Sci. Technol. B* **2005**, *23*, 2963.
(12) Schulz, H.; Wissen, M.; Bogdanski, N.; Scheer, H. C.; Mattes, K.; Friedrich, C. *Microelectron. Eng*. **2006**, *83*, 259.
(13) Ding, Y. F.; Ro, H. W.; Alvine, K. J.; Okerberg, B. C.; Zhou, J.; Douglas, J. F.; Karim, A.; Soles, C. L. *Adv. Funct. Mater*. **2008**, *18*, 1854.
(14) Ding, Y. F.; Ro, H. W.; Douglas, J. F.; Jones, R. L.; Hine, D. R.; Karim, A.; Soles, C. L. *Adv. Mater*. **2007**, *19*, 1377.
(15) Ding, Y. F.; Ro, H. W.; Germer, T. A.; Douglas, J. F.; Okerberg, B. C.; Karim, A.; Soles, C. L. *ACS Nano* **2007**, *1*, 84.
(16) Ryu, J. H.; Lee, T. H.; Oh, S. H.; Cho, S. U.; Kim, C. S.; Jeong, M. Y. *Curr. Appl. Phys*. **2009**, *9*, E7.
(17) Jung, G. Y.; Li, Z. Y.; Wu, W.; Chen, Y.; Olynick, D. L.; Wang, S. Y.; Tong, W. M.; Williams, R. S. *Langmuir* **2005**, *21*, 1158.
(18) Beers, K. L.; Douglas, J. F.; Amis, E. J.; Karim, A. *Langmuir* **2003**, *19*, 3935.
(19) Alvine, K. J.; Ding, Y. F.; Douglas, J. F.; Ro, H. W.; Okerberg, B. C.; Karim, A.; Soles, C. L. *Soft Matter* **2009**, *5*, 2913.
(20) Mullins, W. W. *J. Appl. Phys*. **1957**, *28*, 333.

(21) Hamdorf, M.; Johannsmann, D. *J. Chem. Phys.* **2000**, *112*, 4262.
(22) Angell, C. A.; Ngai, K. L.; McKenna, G. B.; McMillan, P. F.; Martin, S. W. *J. Appl. Phys.* **2000**, *88*, 3113.
(23) Majeste, J. C.; Montfort, J. P.; Allal, A.; Marin, G. *Rheol. Acta* **1998**, *37*, 486.
(24) Schulz, H.; Wissen, M.; Bogdanski, N.; Scheer, H. C.; Mattes, K.; Friedrich, C. *Microelectron. Eng.* **2005**, *78*−*79*, 625.
(25) Ferry, J. D. *Viscoelastic Properties of Polymers*, 3rd ed.; John Wiley & Sons: New York, 1980.
(26) Robertson, C. G.; Warren, S.; Plazek, D. J.; Roland, C. M. *Macromolecules* **2004**, *37*, 10018.
(27) O'Connell, P. A.; McKenna, G. B. *Science* **2005**, *307*, 1760.
(28) Rowland, H.; King, W. P.; Pethica, J. B.; Cross, G. L. W. *Science* **2008**, *322*, 720.
(29) Rowland, H. D.; King, W. P. *J. Micromech. Microeng.* **2004**, *14*, 1625.
(30) Rowland, H. D.; Sun, A. C.; Schunk, P. R.; King, W. P. *J. Micromech. Microeng.* **2005**, *15*, 2414.
(31) Dichtl, M. A.; Sackmann, E. *Proc. Natl. Acad. Sci. U. S. A.* **2002**, *99*, 6533.
(32) Douglas, J. F.; Hubbard, J. B. *Macromolecules* **1991**, *24*, 3163.
(33) Douglas, J. F. *J. Phys.-Condes. Matter* **1999**, *11*, A329.
(34) McKelvey, J. M. *Polymer Processing*; John Wiley & Sons: New York, 1962.
(35) Larson, R. G. *Constitutive Equations for Polymer Melts and Solutions*; Butterworth-Heinemann: Boston, 1988.
(36) Bird, R. B.; Armstrong, R. C.; Hassager, O. *Dynamics of Polymer Liquids*, 2nd ed.; John Wiley & Sons: New York, 1987.
(37) Porter, R. S.; Johnson, J. F. *J. Appl. Phys.* **1961**, *32*, 2326.
(38) Fetters, L. J.; Lohse, D. J.; Richter, D.; Witten, T. A.; Zirkel, A. *Macromolecules* **1994**, *27*, 4639.
(39) Bandyopadhyay, R.; Liang, D.; Yardimci, H.; Sessoms, D. A.; Borthwick, M. A.; Mochrie, S. G. J.; Harden, J. L.; Leheny, R. L. *Phys. Rev. Lett.* **2004**, *93*, 228302.
(40) Cipelletti, L.; Manley, S.; Ball, R. C.; Weitz, D. A. *Phys. Rev. Lett.* **2000**, *84*, 2275.
(41) Narayanan, S.; Lee, D. R.; Hagman, A.; Li, X. F.; Wang, J. *Phys. Rev. Lett.* **2007**, *98*, 185506.
(42) Alvine, K. J.; Ding, Y. F.; Douglas, J. F.; Ro, H. W.; Okerberg, B. C.; Karim, A.; Lavery, K. A.; Lin-Gibson, S.; Soles, C. L. *J. Polym. Sci., Part B: Polym. Phys.* **2009**, *47*, 2591.
(43) Tsui, O. K. C.; Wang, Y. J.; Lee, F. K.; Lam, C. H.; Yang, Z. *Macromolecules* **2008**, *41*, 1465.
(44) Huang, Z. Y.; Hong, W.; Suo, Z. *Phys. Rev. E* **2004**, *70*, 030601.
(45) Huang, Z. Y.; Hong, W.; Suo, Z. *J. Mech. Phys. Solids* **2005**, *53*, 2101.
(46) Huang, R. *J. Mech. Phys. Solids* **2005**, *53*, 63.
(47) Im, S. H.; Huang, R. *J. Appl. Mech.-Trans. ASME* **2005**, *72*, 955.
(48) Im, S. H.; Huang, R. *J. Mech. Phys. Solids* **2008**, *56*, 3315.
(49) Chan, E. P.; Page, K. A.; Im, S. H.; Patton, D. L.; Huang, R.; Stafford, C. M. *Soft Matter* **2009**, *5*, 4638.
(50) Dalby, M. J.; Gadegaard, N.; Tare, R.; Andar, A.; Riehle, M. O.; Herzyk, P.; Wilkinson, C. D. W.; Oreffo, R. O. C. *Nat. Mater.* **2007**, *6*, 997.
(51) Feng, X. J.; Jiang, L. *Adv. Mater.* **2006**, *18*, 3063.
(52) Yi, Y.; Lombardo, G.; Ashby, N.; Barberi, R.; Maclennan, J. E.; Clark, N. A. *Phys. Rev. E* **2009**, *79*, 041701.